

# Molecular hydrogen and its proxies HCO<sup>+</sup> and CO in the diffuse interstellar medium

HARVEY LISZT<sup>1</sup> AND MARYVONNE GERIN<sup>2</sup>

<sup>1</sup>*National Radio Astronomy Observatory  
520 Edgemont Road, Charlottesville, VA 22903  
hliszt@nrao.edu*

<sup>2</sup>*LERMA, Observatoire de Paris, PSL Research University,  
CNRS, Sorbonne Université  
maryvonne.gerin@observatoiredeparis.psl.eu*

## ABSTRACT

There is a robust polyatomic chemistry in diffuse, partially-molecular interstellar gas that is readily accessible in absorption at radio/mm/sub-mm wavelengths. Accurate column densities are derived owing to the weak internal excitation, so relative molecular abundances are well known with respect to each other but not with respect to H<sub>2</sub>. Here we consider the use of proxies for hydrogen column densities N(H<sub>2</sub>) and N(H) = N(HI)+2N(H<sub>2</sub>) based on measurements of HCO<sup>+</sup> absorption and CO emission and absorption, and we compare these with results obtained by others when observing HI, H<sub>2</sub> and CO toward stars and AGN. We consider the use of HCO<sup>+</sup> as a proxy for H<sub>2</sub> and show that the assumption of a relative abundance N(H<sub>2</sub>) = N(HCO<sup>+</sup>)/3 × 10<sup>-9</sup> gives the same view of the atomic-molecular hydrogen transition that is seen in UV absorption toward stars. CO on the other hand shows differences between the radio and optical regimes because emission is always detected when N(HCO<sup>+</sup>) ≥ 6 × 10<sup>11</sup> cm<sup>-2</sup> or N(H<sub>2</sub>) ≥ 2 × 10<sup>20</sup> cm<sup>-2</sup>. Wide variations in the integrated CO J=1-0 brightness W<sub>CO</sub> and N(CO)/N(H<sub>2</sub>) imply equivalent variations in the CO-H<sub>2</sub> conversion factor even while the ensemble mean is near the usual Galactic values. Gas/reddening ratios found in absorption toward stars, N(H)/E(B-V) = 6.2 × 10<sup>21</sup> H cm<sup>-2</sup> (mag)<sup>-1</sup> overall or 6.8 × 10<sup>21</sup> H cm<sup>-2</sup> (mag)<sup>-1</sup> for sightlines at E(B-V) ≤ 0.08 mag lacking H<sub>2</sub> are well below the Galactic mean measured at low reddening and high Galactic latitude, 8.3 × 10<sup>21</sup> H cm<sup>-2</sup> (mag)<sup>-1</sup>.

*Keywords:* astrochemistry . ISM: dust . ISM: HI. ISM: clouds

## 1. INTRODUCTION

The discovery of *c*-C<sub>3</sub>H<sub>2</sub> and HCO<sup>+</sup> at radio frequencies (Cox et al. 1988; Lucas & Liszt 1993) pointed the way to an unexpectedly accessible and complex absorption line chemistry of diffuse inter-

stellar gas seen along sightlines having extinction A<sub>V</sub> ≤ 1 mag. The molecular inventory now includes more than three dozen species as complex as H<sub>2</sub>CO, NH<sub>3</sub> (Nash 1990; Liszt et al. 2006) and CH<sub>3</sub>CN (Liszt et al. 2018a). There is a wide range neutral hydrides and hydride ions (Gerin et al. 2016), linear and cyclic hydrocarbons CH, C<sub>2</sub>H, C<sub>3</sub>H and C<sub>3</sub>H<sub>2</sub> (Lucas & Liszt 2000; Liszt et al.

2012, 2018a), sulfur compounds CS, SO, H<sub>2</sub>S, SH and HCS<sup>+</sup> (Lucas & Liszt 2002; Neufeld et al. 2015). There is a diverse group of molecular ions CH<sup>+</sup>, HOC<sup>+</sup>, CF<sup>+</sup> and C<sub>3</sub>H<sup>+</sup>, (Gerin et al. 2019) in addition to HCO<sup>+</sup> whose use as a tracer of H<sub>2</sub> is the subject of this work. A recent search for CO<sup>+</sup> was unsuccessful (Gerin & Liszt 2021).

Half of the diatomics detected in diffuse gas are observed in UV/optical absorption but among the polyatomics only a few are observed outside the radio waveband, including C<sub>3</sub> in the optical (Maier et al. 2001) and H<sub>3</sub><sup>+</sup> in the near IR (Geballe & Oka 1996). Only CO, OH, and CH are widely observable in emission. For this reason the range of the diffuse gas chemistry is accessible only in absorption on sightlines toward radio continuum sources that are widely separated over the sky and only seldom are bright enough to observe spectroscopically at both optical and radio wavelengths (Liszt 2021).

This has the consequence that the abundances of the molecules observed at radio wavelengths are well-determined and known with respect to each other but not directly known with respect to molecular hydrogen. However, CH, OH and CO are observed in UV/optical absorption toward stars along with H<sub>2</sub>, and they are also observable at radio/sub-mm frequencies. The relative abundances  $X(\text{CH}) = N(\text{CH})/N(\text{H}_2) = 3.5 \times 10^{-8}$  (Sheffer et al. 2008; Weselak et al. 2010) and  $X(\text{OH}) = N(\text{OH})/N(\text{H}_2) = 10^{-7}$  (Weselak et al. 2010) are observed to be fixed in UV/optical absorption, with the consequence that the relative abundance  $X(\text{HCO}^+) = N(\text{HCO}^+)/N(\text{H}_2) = 3.0 \times 10^{-9}$  is also known with a logarithmic uncertainty of 0.2 dex (Gerin et al. 2019).

The existence of a trusted HCO<sup>+</sup>/H<sub>2</sub> ratio puts the polyatomic diffuse cloud chemistry on a firmer basis and in two recent works we explored the use of HCO<sup>+</sup> to assess the molecular component of the dark neutral medium (DNM) (Planck Collaboration et al. 2015; Remy et al. 2018) in the outskirts of the

Chamaeleon clouds (Liszt et al. 2018b). We found that the DNM was mostly molecular even while the medium as a whole was predominantly atomic. We explained the absence of CO emission associated with the DNM as the result of very low CO/H<sub>2</sub> relative abundances as determined in CO and HCO<sup>+</sup> absorption (Liszt et al. 2019).

We have since acquired many more ALMA and IRAM 30m measurements of HCO<sup>+</sup> and CO along directions in the outer Galaxy and in forthcoming work we will use that data to study the DNM and the chemical properties of diffuse gas. Before doing so, we explore further the underpinnings of our program and the determination of hydrogen column densities  $N(\text{HI})$ ,  $N(\text{H}_2)$  and  $N(\text{H}) = N(\text{HI}) + 2N(\text{H}_2)$  in diffuse molecular gas. We compare and merge observations of H<sub>2</sub> and its proxies HCO<sup>+</sup> and CO along the various sightlines on which they have been observed in their respective wavebands. We ask whether we are getting the same idea of H<sub>2</sub> formation in diffuse gas (Bellomi et al. 2020) from observations in the UV/optical and radio domains, and whether we are tracing the same chemical behaviour in different environments. To do so we need a common medium of exchange which we chiefly find in the reddening,  $E(\text{B}-\text{V})$ , that is determined photometrically toward stars and inferred from far infrared emission otherwise.

Results of observations in either domain in different directions can be plotted against reddening whether determined spectroscopically toward a background star or using the all-sky maps of the FIR-determined optical reddening equivalent (Schlegel et al. 1998). In turn, the reddening is commonly used as a proxy for the total column density of H-nuclei in neutral atoms and molecules,  $N(\text{H}) = N(\text{HI}) + 2N(\text{H}_2)$ , offering the possibility of determining the fraction of hydrogen in molecular form. The atomic and molecular components of  $N(\text{H})$  are observable along the sightlines used in UV absorption while the atomic component  $N(\text{HI})$  is globally visible in  $\lambda 21\text{cm}$

emission, including at  $E(B-V) \lesssim 0.1$  mag where  $N(H_2)$  is negligible. Somewhat surprisingly, it is found [Liszt \(2014a,b\)](#) that the  $N(HI)/E(B-V)$  ratio at  $\lambda 21$ cm at low  $E(B-V)$  (and perforce at high galactic latitudes),  $8.3 \times 10^{21} \text{ HI cm}^{-2} (\text{mag})^{-1}$ , is 40% larger than the canonical value  $N(H)/E(B-V) = 5.8 \times 10^{21} \text{ H-nuclei cm}^{-2} (\text{mag})^{-1}$  determined by [Bohlin et al. \(1978\)](#) toward stars. Here we show that a small part of the difference can be ameliorated at low reddening using the most recent observations of  $N(HI)$  toward early-type stars, while the 40% difference is confirmed overall and especially at  $E(B-V) \gtrsim 0.1$  mag where  $N(H_2)$  is appreciable and the  $N(H)-E(B-V)$  relation toward stars is tighter and more robust.

The work is arranged as follows: Section 2 is a summary of the observational materials discussed. Section 3 discusses variations in the UV-derived  $N(HI)$  and  $N(H_2)$  with respect to  $E(B-V)$  and each other. Section 4 merges the UV absorption and mm-wave measurements of  $H_2$  and CO. Section 5 is a summary.

## 2. DATASETS EMPLOYED HERE

### 2.1. UV absorption

#### 2.1.1. $H_2$

We include previously published measurements of  $N(H_2)$  toward bright stars by [Bohlin et al. \(1978\)](#), [Burgh et al. \(2007\)](#), [Sheffer et al. \(2008\)](#), [Rachford et al. \(2009\)](#) and [Shull et al. \(2021\)](#) and detections of  $N(H_2)$  in UV absorption against 34 optically bright AGN at low reddening by [Gillmon et al. \(2006\)](#).

#### 2.1.2. $HI$

The references cited in Section 2.1.1 reporting measurements of  $N(H_2)$  in UV absorption toward bright stars typically have complementary measured values of  $N(HI)$  measured in Lyman- $\alpha$  absorption, with occasional exceptions. [Bohlin et al. \(1978\)](#) used the  $N(HI)$  values of [Savage et al. \(1977\)](#). [Diplas & Savage \(1994\)](#) reported a survey of Ly- $\alpha$  measurements of  $N(HI)$  toward 554

stars using IUE and this dataset was used to fill gaps in the entries for  $N(HI)$  in [Sheffer et al. \(2008\)](#) and [Shull et al. \(2021\)](#) where possible. Such sightlines are attributed to [Sheffer et al. \(2008\)](#) or [Shull et al. \(2021\)](#) as appropriate. The data of [Diplas & Savage \(1994\)](#) are used here along sightlines that do not have measured values of  $N(H_2)$ .

Uniquely, [Gillmon et al. \(2006\)](#) reported  $N(HI)$  measured in  $\lambda 21$ cm emission, from the survey of [Wakker et al. \(2001\)](#) as noted in Section 2.2.4. Their survey of 45 sightlines included 38 with measured  $N(HI)$  and 7 with lower limits.

### 2.1.3. CO

We include measurements of  $N(CO)$  in UV absorption toward bright stars from [Burgh et al. \(2007\)](#), [Sonnentrucker et al. \(2007\)](#), [Sheffer et al. \(2007\)](#) and [Sheffer et al. \(2008\)](#), which we have considered in other recent references, especially [Liszt \(2017, 2020\)](#).

## 2.2. Radio frequency data

### 2.2.1. The $H_2$ surrogate $HCO^+$

We include previously reported values of  $N(HCO^+)$  from [Lucas & Liszt \(1996\)](#), [Liszt & Lucas \(2000\)](#), [Liszt & Gerin \(2018\)](#) and [Liszt et al. \(2018b\)](#) measured in absorption toward bright compact extragalactic mm-wave continuum sources. Also included and reported here for the first time are Cycle 6 ALMA results of the same kind in 33 directions toward ALMA phase calibrators seen in the outer Galaxy, which resulted in 28 detections. As in [Liszt & Gerin \(2018\)](#) and [Liszt et al. \(2018b\)](#), these are products of the regular pipeline, taken from the resultant datacubes at the peak of the continuum. The profile-integrated optical depth of  $HCO^+$  in units of  $\text{km s}^{-1}$  is denoted by  $\Upsilon_{HCO^+}$ .

### 2.2.2. CO emission

Reported here for the first time in Table 1 are line profile integrals  $W_{CO}$  from IRAM CO J=1-0 emission profiles taken in a frequency-switching mode in August 2019 toward those 28 of the new 33 outer

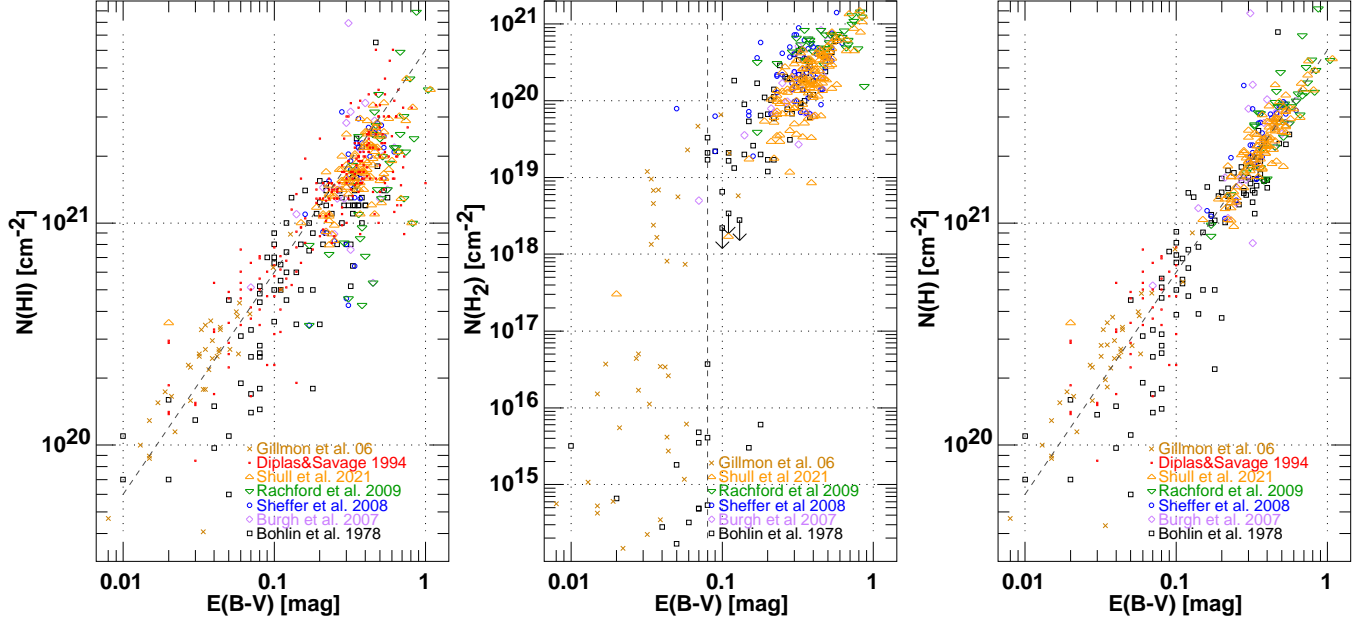


**Figure 1.**  $N(\text{HI})$ ,  $N(\text{H}_2)$  and  $N(\text{H}) = N(\text{HI}) + 2N(\text{H}_2)$  plotted against reddening as discussed in Section 2.3. Shown at left and right are dashed gray lines at  $N(\text{HI})/E(B-V)$  and  $N(\text{H})/E(B-V) = 6 \times 10^{21} \text{ cm}^{-2} \text{ mag}^{-1}$  respectively, near the canonical value of [Bohlin et al. \(1978\)](#). Shown in the middle is a vertical dashed grey line at  $E(B-V) = 0.08$  mag where  $N(\text{H}_2)$  canonically turns on in the diffuse ISM. Most upper limits on  $N(\text{H}_2)$  are not physically meaningful and have been suppressed but a few are shown in the middle panel to indicate that lines of sight with low  $N(\text{H}_2)$  are occasionally seen even at  $E(B-V) > 0.1$  mag. Also shown at right are values of  $N(\text{HI})$  from [Diplas & Savage \(1994\)](#) at  $E(B-V) \leq 0.1$  mag where the molecular hydrogen fraction is small.  $N(\text{HI})$  from [Diplas & Savage \(1994\)](#) are only shown for sightlines lacking measured values of  $N(\text{H}_2)$ . The numbers of datapoints shown from left to right are 561, 370 and 381.

Galaxy sightlines with detected  $\text{HCO}^+$ . Five-point maps were made around each direction, pointing toward the target and displaced by 1.2 half-power beamwidths ( $1.2 \times 22''$ ) in the four cardinal directions, and the profiles were co-added to produce the results shown here. The intensity scale is the usual main-beam intensity scale of the standard output.

Also reported here are older ARO Kitt Peak 12m results that had accumulated over the past several decades and were previously reported in [Liszt et al. \(2010\)](#) and [Liszt & Pety \(2012\)](#).

### 2.2.3. $N(\text{CO})$ measured in emission and/or absorption

[Liszt & Lucas \(1998\)](#) measured  $N(\text{CO})$  using a combination of profiles of the  $J=1=0$  and  $J=2-1$  lines measured in  $^{12}\text{CO}$  and  $^{13}\text{CO}$ . [Liszt et al. \(2018b\)](#) extrapolated the methods of [Liszt & Lucas \(1998\)](#) to measure  $N(\text{CO})$  toward 6 directions in

Chamaeleon from observations of  $J=1-0$   $^{12}\text{CO}$  absorption.

### 2.2.4. $N(\text{HI})$ measured in $\lambda 21\text{cm}$ emission

In the absence of Lyman- $\alpha$  measurements in absorption toward AGN, [Gillmon et al. \(2006\)](#) determined  $N(\text{HI})$  in  $\lambda 21\text{cm}$  emission from the high-velocity cloud survey of [Wakker et al. \(2001\)](#).

## 2.3. Reddening $E(B-V)$

Observations of UV absorption toward bright stars report values for the optical reddening  $E(B-V)$  derived photometrically from stellar spectra. In the UV absorption survey of  $\text{H}_2$  toward AGN [Gillmon et al. \(2006\)](#) and for sightlines observed in CO and  $\text{HCO}^+$  at mm-wavelengths, values of  $E(B-V)$  were taken from [Schlegel et al. \(1998\)](#). As noted in Section 3, recent measurements of  $N(\text{HI})$  plotted against these two measures

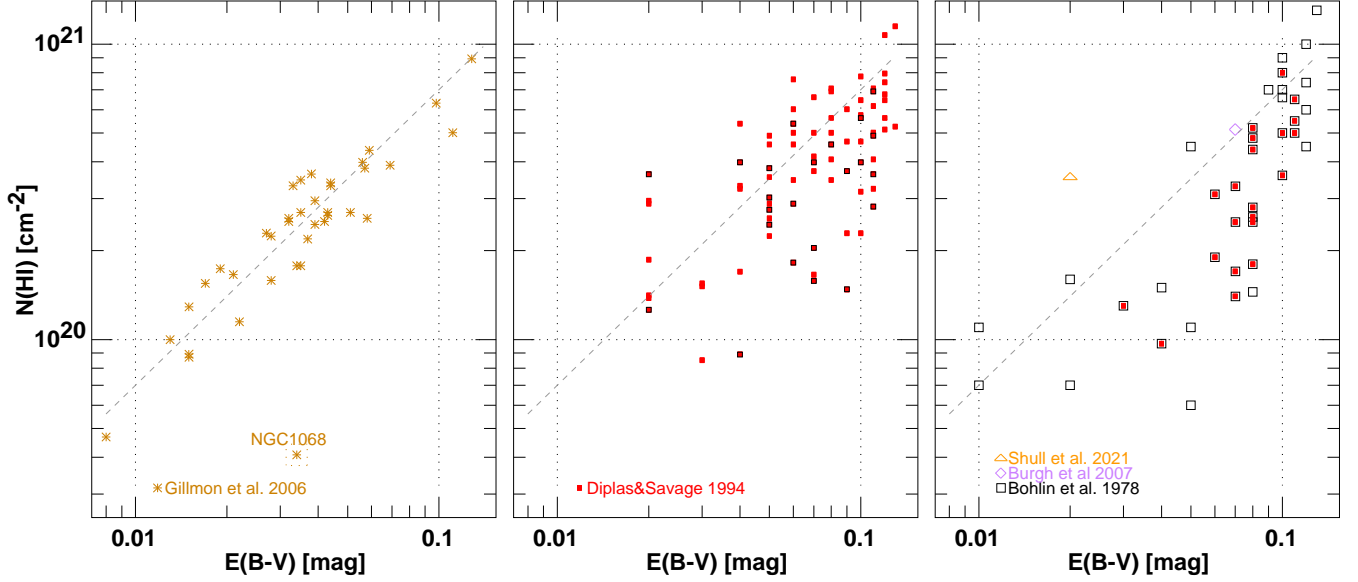


**Figure 2.**  $N(\text{HI})$  at low reddening. Left: from Gillmon et al. (2006) using  $E(B-V)$  from Schlegel et al. (1998) and  $N(\text{HI})$  from  $\lambda 21\text{cm}$  emission. Middle and right: from Diplaz & Savage (1994) and Bohlin et al. (1978), respectively, using  $E(B-V)$  from stellar photometry and  $N(\text{HI})$  from stellar Lyman- $\alpha$  absorption. The dashed grey line in each panel is drawn at  $N(\text{HI})/E(B-V) = 7 \times 10^{21} \text{ cm}^{-2} \text{ mag}^{-1}$ , higher than the comparable lines drawn in Figure 1. Sightlines common to the samples of Diplaz & Savage (1994) and Bohlin et al. (1978) are noted by black outlining in the middle panel and red fill at right: they have the same  $N(\text{HI})$  and different  $E(B-V)$  in the two references as remarked in Appendix C. Results extracted from these samples are presented in Table 2.

show very similar mean  $N(\text{HI})/E(B-V)$  but very different systematic behaviour.

#### 2.4. Summary

The means by which our references derive their values for  $E(B-V)$ ,  $N(\text{HI})$ ,  $N(\text{H}_2)$  and  $N(\text{CO})$  are summarized in Table 4 in Appendix A. The new CO and  $\text{HCO}^+$  profiles used in this work are described in Appendix B and shown in Figure 7.

### 3. RELATIONSHIPS AMONG UV-MEASURED QUANTITIES

We wish to use the reddening  $E(B-V)$  to infer  $N(\text{H})$  along sightlines studied at radio wavelengths and as a means of comparing observed and inferred results for  $N(\text{H}_2)$  between optical and radio wavebands, respectively. Ascertaining the  $N(\text{H})/E(B-V)$  ratio took on new interest when it was realized that  $N(\text{H})/E(B-V)$  could be substantially larger than the widely-used UV/optical-determined value  $5.8 \times 10^{21} \text{ cm}^{-2} \text{ H-nuclei (mag)}^{-1}$  (Bohlin et al. 1978) when sampled in  $\lambda 21\text{cm}$  HI emission at Galactic

latitudes above  $20^\circ$  (Liszt 2014a,b). Those references found a 40% larger value  $N(\text{H})/E(B-V) = 8.3 \times 10^{21} \text{ H-nuclei cm}^{-2} \text{ (mag)}^{-1}$ . Other recent studies find or use ratios  $N(\text{H})/E(B-V) = 7.7 - 9.4 \times 10^{21} \text{ H-nuclei cm}^{-2} \text{ (mag)}^{-1}$  (Hensley & Draine 2017; Lenz et al. 2017; Li et al. 2018). Hensley & Draine (2021) use  $8.8 \times 10^{21} \text{ H-nuclei cm}^{-2} \text{ (mag)}^{-1}$ .

#### 3.1. $N(\text{HI})/E(B-V)$ and $N(\text{H})/E(B-V)$

The variations of  $N(\text{H})$  and its constituents  $N(\text{HI})$  and  $N(\text{H}_2)$  determined in UV absorption are shown with respect to  $E(B-V)$  in Figure 1. Shown at left and right is a line representing a column density/reddening ratio  $N(\text{HI})/E(B-V)$  or  $N(\text{H})/E(B-V) = 6 \times 10^{21} \text{ H-nuclei cm}^{-2} \text{ (mag)}^{-1}$ , ie the old standard value. Comparing the panels at left and right for  $N(\text{HI})$  and  $N(\text{H})$ , it is striking how summing the atomic and molecular contributions tightens the column density-reddening relationship at  $E(B-V) \gtrsim 0.1$ , removing for instance most of the very large scatter in  $N(\text{HI})$



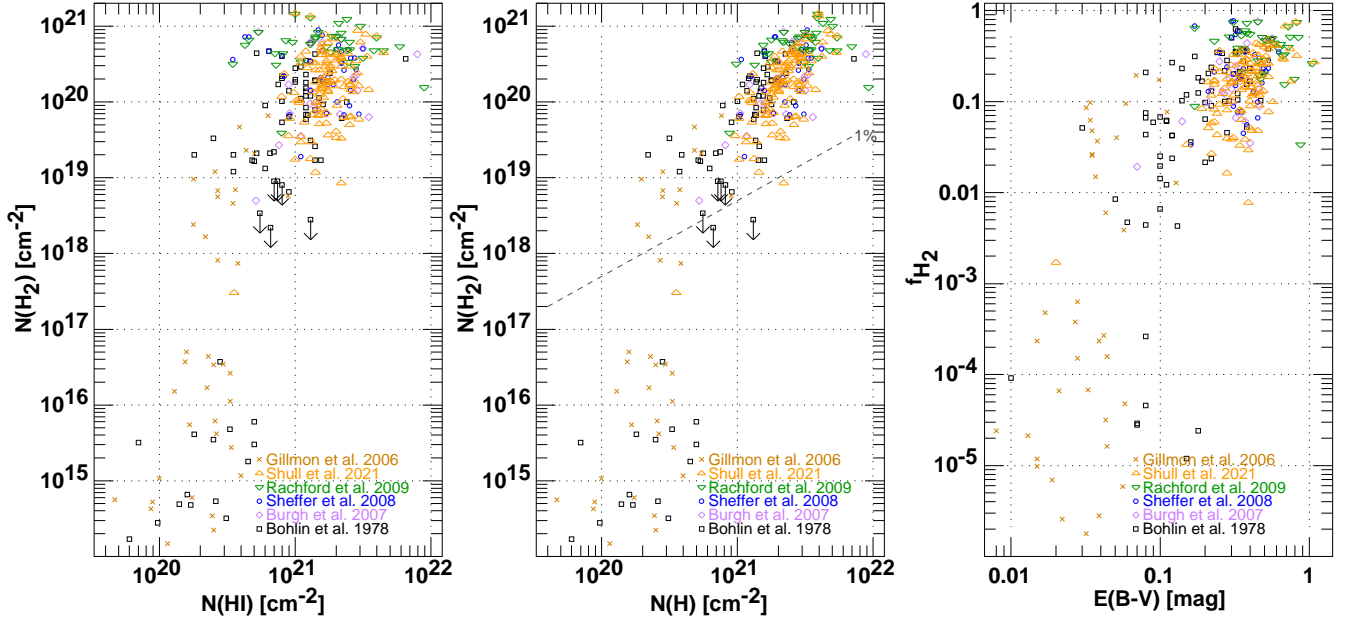


**Figure 3.**  $N(\text{H}_2)$  plotted against  $N(\text{HI})$  and  $N(\text{H})$  at left and middle, and the molecular hydrogen fraction plotted against reddening at right. As in Figure 2 a few physically significant upper limits on  $N(\text{H}_2)$  are shown to indicate that the appearance of sightlines with small  $N(\text{H}_2)$  extends to somewhat higher  $N(\text{HI})$  and  $N(\text{H})$  than might otherwise be apparent. 318, 318 and 323 points representing measurements are shown in the panels from left to right, respectively. The ensemble mean molecular fraction for all measurements is  $\langle f_{\text{H}_2} \rangle = 0.20$  and  $f_{\text{H}_2} = 0.24 \pm 0.16$  in a narrow interval around  $E(\text{B-V}) = 0.32$  mag corresponding to  $A_V = 1$  mag. The dashed line in the middle panel shows the locus corresponding to  $f_{\text{H}_2} = 0.01$ .

around  $E(\text{B-V}) \approx 0.3 - 0.4$  mag in the strongly molecular sample of Rachford et al. (2009). Moreover, the old standard ratio  $N(\text{H})/E(\text{B-V}) = 5.8 \times 10^{21} \text{ H-nuclei cm}^{-2} (\text{mag})^{-1}$  is a good representation of the more strongly-molecular data at  $E(\text{B-V}) \gtrsim 0.2$  mag, as noted recently by Shull et al. (2021).

The regression lines for all the data and for  $E(\text{B-V}) \geq 0.2$  mag are the same in Figure 1 at right, with power-law slopes of 1.0 and  $N(\text{H})/E(\text{B-V}) = 6.2 \times 10^{21} \text{ H-nuclei cm}^{-2} (\text{mag})^{-1}$ . This is only 6% higher than the old standard value and 2% larger than the quantity calculated by Shull et al. (2021)  $\langle N(\text{H}_2)/E(\text{B-V}) \rangle = (6.07 \pm 1.01) \times 10^{21} \text{ cm}^{-2} (\text{mag})^{-1}$ .

The absence of a tighter column density-reddening relationship in atomic and weakly-molecular gas at  $E(\text{B-V}) \lesssim 0.2$  mag in Figure 1 is something of a puzzle, given the lack of competition for H-nuclei between atomic and molecular hydrogen. At high Galactic latitude and small reddening where  $\text{H}_2$  is unimportant, the col-

umn density-reddening relationship determined in  $\lambda 21\text{cm}$  HI emission is tight down to  $E(\text{B-V}) = 0.01$  mag meaning that the contribution of  $\text{H}^+$  is not important.

To explore this, Figure 2 shows expanded plots of  $N(\text{HI})$  against reddening at  $E(\text{B-V}) \lesssim 0.1$  mag for the different datasets. The data of Gillmon et al. (2006) using the IR-determined reddening and  $N(\text{HI})$  measured in  $\lambda 21\text{cm}$  emission are shown separately at left: The other datasets use stellar reddening and  $N(\text{HI})$  measured in Ly- $\alpha$  absorption. The IUE data of Diplas & Savage (1994) are shown in the middle while the rest of the UV absorption line measurements of  $N(\text{HI})$ , almost all from the original *Copernicus* sample of Bohlin et al. (1978), are shown at right. There is a variety of different behaviour and the statistics of the data at  $E(\text{B-V}) \leq 0.08$  mag are summarized in Table 2.

The  $N(\text{HI})$ - $E(\text{B-V})$  relationship is only tight in the highly-ordered dataset of Gillmon et al. (2006)

that does not use stellar measurements. The data appear to depart from a simple linear relation at higher  $E(B-V)$  where  $N(H_2)$  may be significant. The data of [Diplas & Savage \(1994\)](#) have a similar ensemble mean  $\langle N(HI) \rangle / \langle E(B-V) \rangle$  to that of [Gillmon et al. \(2006\)](#) at slightly higher  $\langle E(B-V) \rangle$  (Table 2) but considerably more scatter. The scatter must in part arise from the limited precision of the quoted reddening, but also from random error in the determination of  $E(B-V)$  from stellar spectra. Comparison of measurements of  $N(HI)$  and  $N(HI)/E(B-V)$  along sightlines observed in common between [Bohlin et al. \(1978\)](#) and [Diplas & Savage \(1994\)](#) in Appendix C leaves little doubt that this is the case.

The two newer datasets of [Diplas & Savage \(1994\)](#) and [Gillmon et al. \(2006\)](#) comprise 80% of the measurements below  $E(B-V) = 0.08$  mag and (see Table 2) have a mean  $\langle N(HI) \rangle / \langle E(B-V) \rangle = 6.8 \times 10^{21} \text{ H-nuclei cm}^{-2} (\text{mag})^{-1}$ . In a log sense this spans about half of the difference between the values  $5.8$  and  $8.3 \times 10^{21} \text{ H-nuclei cm}^{-2} (\text{mag})^{-1}$ . The dataset of [Bohlin et al. \(1978\)](#) has 40% lower ensemble mean  $\langle N(HI) \rangle / \langle E(B-V) \rangle = 4.1 \times 10^{21} \text{ cm}^{-2} (\text{mag})^{-1}$  than the newer data. A more detailed comparison is given in Appendix C.

We summarize these results by concluding first that  $N(HI)/E(B-V)$  measured at low extinction, and  $N(H)/E(B-V)$  overall, are smaller than the mean  $N(HI)/E(B-V)$  determined from  $\lambda 21\text{cm}$  emission above latitude  $20^\circ$  for the Galaxy at large. As shown in Table 2, a new value of  $\langle N(H) \rangle / E(B-V)$  derived from the four times larger dataset shown in Figure 1 at all  $E(B-V)$  would be  $\langle N(H) \rangle / \langle E(B-V) \rangle = 6.2 \times 10^{21} \text{ H-nuclei cm}^{-2} (\text{mag})^{-1}$ , an increase of only 7% over that of [Bohlin et al. \(1978\)](#). At the same time, the mean gas/reddening ratio  $N(HI)/E(B-V)$  at  $E(B-V) \leq 0.08$  mag in Table 2,  $6.8 \times 10^{21} \text{ H-nuclei cm}^{-2} (\text{mag})^{-1}$ , is larger than the mean over all reddening but still smaller than the comparable high-latitude Galactic average.

### 3.2. $N(H_2)$ vs reddening

The behaviour of  $N(H_2)$  with  $E(B-V)$  is shown in the middle panel of Figure 1. Subsequent to the original survey of [Bohlin et al. \(1978\)](#), observers of H<sub>2</sub> toward bright stars studied sightlines with appreciable  $N(H_2)/N(H)$ . This has the somewhat unfortunate consequence that the rise of  $N(H_2)$  at small  $E(B-V)$  is largely documented in the sightlines of [Gillmon et al. \(2006\)](#) toward AGN that represent different conditions and/or a different reddening measurement method from the bulk of the data overall. As can be seen in Figure 1, a few sightlines with small  $N(H_2)$  persist up to  $E(B-V) \lesssim 0.2$  mag. but in general, sightlines with  $N(H_2) \ll 10^{19} \text{ cm}^{-3}$  at  $E(B-V) > 0.08$  mag are rare.

### 3.3. Variation of $N(H_2)$ and the molecular fraction with $N(HI)$ and $N(H)$

For completeness and to facilitate consideration of the molecular fraction, Figure 3 shows the variation of  $N(H_2)$  with respect to  $N(HI)$  and  $N(H)$ . The variation of the molecular fraction  $f_{H_2} = 2N(H_2)/(N(HI) + 2N(H_2))$  with  $N(H)$  is implicit in the middle panel of Figure 3 and the variation of  $f_{H_2}$  with  $E(B-V)$  is shown at right there. [Bellomi et al. \(2020\)](#) recently used a version of the middle panel in Figure 3, with data compiled by [Gudennavar et al. \(2012\)](#) lacking the recent sample of [Shull et al. \(2021\)](#), to show that the statistics of H<sub>2</sub> formation can be reproduced in a simulation of the turbulent ISM.

The ensemble mean molecular fraction for all the data in Figure 3 is  $\langle f_{H_2} \rangle = 0.20$ . The mean molecular fraction in a narrow interval  $A_V = 0.95 - 1.05$  mag, with  $A_V = 3.1 E(B-V)$ , is only slightly larger  $0.24 \pm 0.16$ .

For reference, recall that a Spitzer “standard HI cloud” [Spitzer \(1978\)](#) has  $N(H) = 4 \times 10^{20} \text{ cm}^{-2}$  and  $E(B-V) = 0.07$  mag, and according to Figures 1 and 3, such a cloud will have a molecular fraction  $f_{H_2}$  of order 1-10%. The equilibrium value of  $f_{H_2}$  at the center of a quiescent HI cloud model resembling the Spitzer Standard Cloud is about one quarter ([Liszt 2007b](#)).

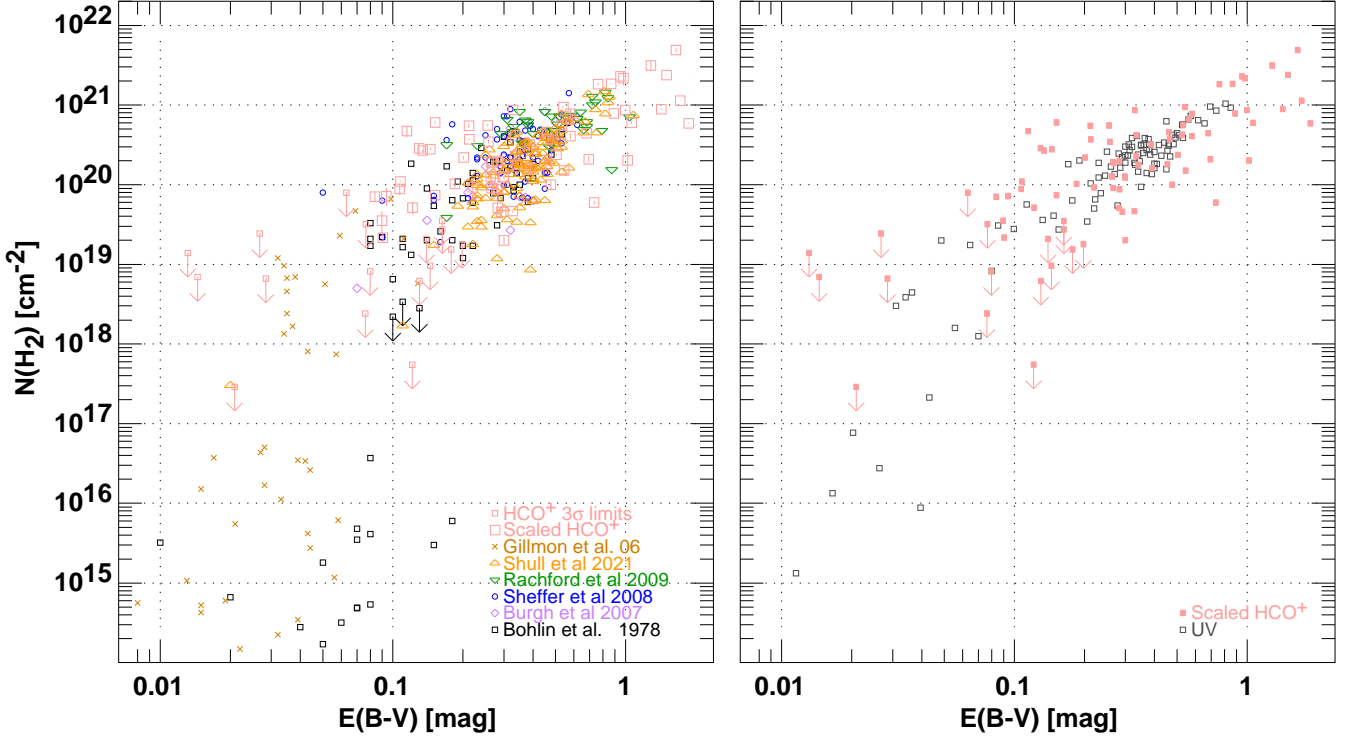


**Figure 4.**  $N(\text{H}_2)$  plotted against reddening, using the data from Figure 1 and merging the UV and mm-wave absorption results by scaling  $N(\text{H}_2) = N(\text{HCO}^+)/3 \times 10^{-9}$ . At right the UV datasets were merged and sorted in  $E(\text{B-V})$ , then averaged horizontally and vertically in sequential non-overlapping groups of four to reduce the scatter and facilitate comparison. See Table 3 for a quantitative comparison.

#### 4. MERGING UV ABSORPTION AND MM-WAVE MEASUREMENTS

To merge the UV/optical and radio datasets we consider two aspects; using  $\text{HCO}^+$  as a proxy for  $\text{H}_2$  and using  $N(\text{CO})$  and  $W_{\text{CO}}$  interchangeably as proxies for each other. If these are possible, the fractional CO abundances and CO- $\text{H}_2$  conversion factors derived in the two regimes may be compared.

##### 4.1. $\text{HCO}^+$ considered as a proxy for $\text{H}_2$

Shown in Figure 4 are the UV/optical absorption measurements of  $N(\text{H}_2)$  plotted against  $E(\text{B-V})$  as in Figure 3, with mm-wave measurements put on the same scale using  $N(\text{H}_2) = N(\text{HCO}^+)/3 \times 10^{-9}$ . At right in Figure 4, the cloud of UV absorption measurements was collapsed to facilitate comparison: The individual UV datasets were merged, the resultant dataset was sorted in  $E(\text{B-V})$  and the

data were averaged horizontally and vertically in sequential non-overlapping groups of four.

On the scale of Figure 4 there is no offset between the radio and UV datasets: the behaviour of  $N(\text{H}_2)$  vs  $E(\text{B-V})$  is the same. Table 3 shows that the ensemble means  $\langle N(\text{H}_2) \rangle / \langle E(\text{B-V}) \rangle$  measured in the UV/optical and radio/IR are within about 0.1 dex (25%) and the properties of the radio data are indistinguishable from those of the three most recent UV absorption studies, especially Rachford et al. (2009) that has comparable  $\langle E(\text{B-V}) \rangle$ . Within the scatter, which is large for both  $N(\text{H}_2)$  and  $N(\text{HCO}^+)$  vs.  $E(\text{B-V})$ ,  $\text{HCO}^+$  is a reliable proxy for  $\text{H}_2$  with the assumption that  $N(\text{H}_2) = N(\text{HCO}^+)/3 \times 10^{-9}$ . Demonstrating the coincidence of the UV and mm-wave determinations of  $N(\text{H}_2)$  is the most important result of this work and was never a foregone conclusion. It is perhaps surprising, considering that the UV absorption measurements sample gas toward rela-



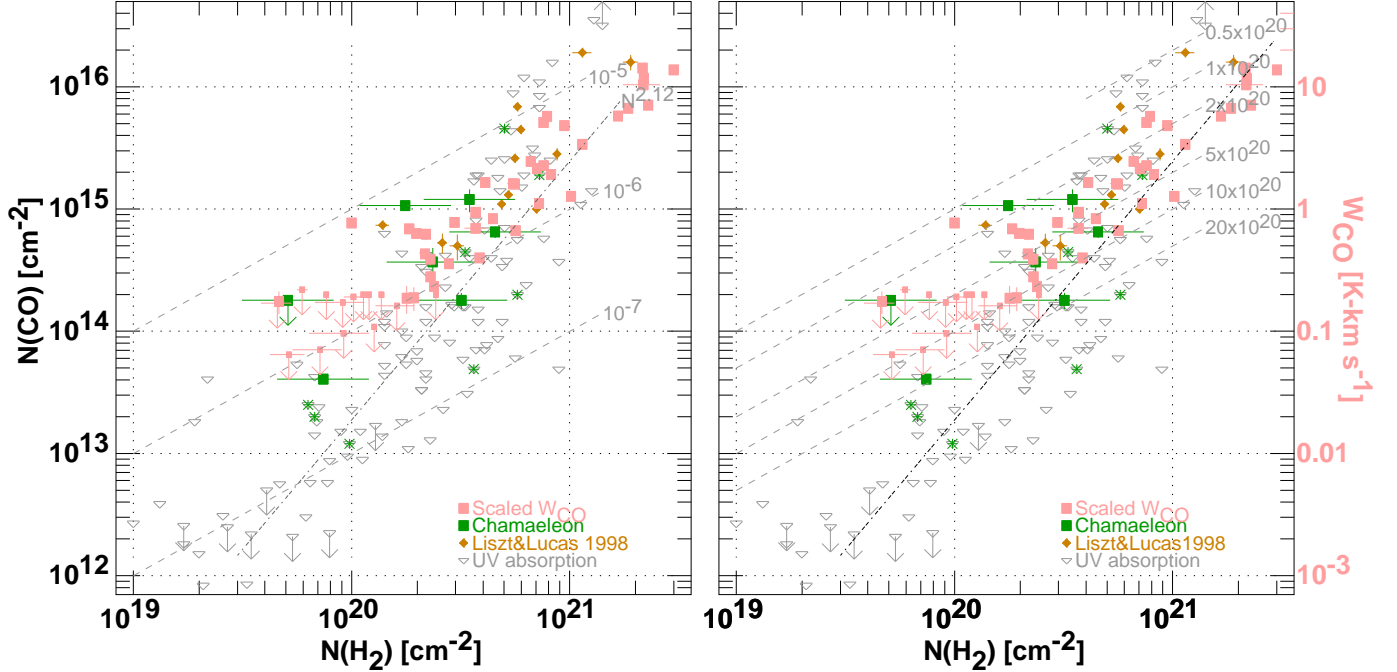


**Figure 5.**  $N(\text{CO})$  and  $W_{\text{CO}}$  plotted against  $N(\text{H}_2)$  merging ratio and optical data with two scalings:  $N(\text{H}_2) = N(\text{HCO}^+)/3 \times 10^{-9}$  and  $N(\text{CO}) = W_{\text{CO}} \times 10^{15} \text{ cm}^{-2} (\text{K-km s}^{-1})^{-1}$ .  $N(\text{CO})$  and  $N(\text{H}_2)$  values derived from UV absorption are plotted as a background of gray downward-pointing open triangles. Symbols shown in green are results from our earlier observations in Chamaeleon (Liszt et al. 2019) with filled rectangles representing  $N(\text{CO})$  derived in  $\lambda 2.6\text{mm}$  absorption and green asterisks marking the positions of 8 Chamaeleon stars in the wider stellar UV absorption sample. Gray dashed lines represent the fractional abundance  $N(\text{CO})/N(\text{H}_2)$  at left and the CO-H<sub>2</sub> conversion factor  $N(\text{H}_2)/W_{\text{CO}}$  at right. The dash-dotted line with power-law slope 2.12 is a regression fit to a portion of the data as discussed in Section 4.2

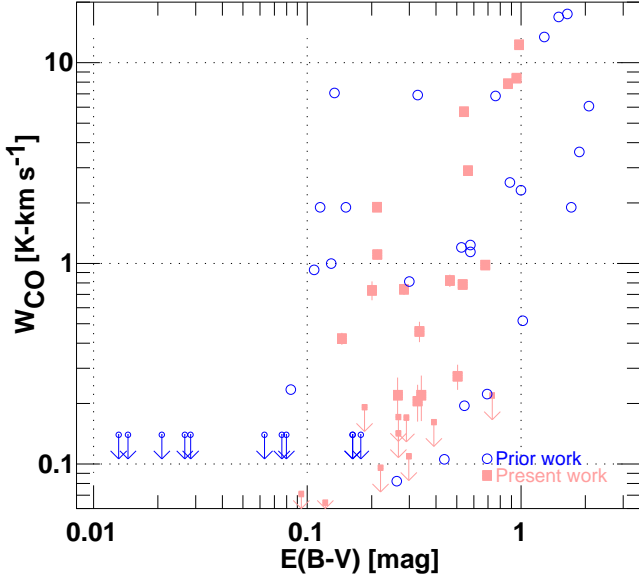


**Figure 6.** CO emission  $W_{\text{CO}}$  plotted against reddening  $E(\text{B-V})$ .

tively rare, early-type stars that are surrounded by natal gas and have a significant influence on their immediate environment. Environmental effects are more clearly manifested when CO is considered,

#### 4.2. $W_{\text{CO}}$ and $N(\text{CO})$ as mutual proxies

In Figure 5 we plot CO column densities and integrated brightness  $W_{\text{CO}}$  against  $N(\text{H}_2)$ , using the usual fractional abundance  $N(\text{HCO}^+)/N(\text{H}_2) = 3 \times 10^{-9}$  and the additional conversion  $W_{\text{CO}} = N(\text{CO})/10^{15} \text{ cm}^{-2}$  in units of  $\text{K-km s}^{-1}$  as in Liszt (2017). This relationship was evident when the J=1-0 and J=2-1 transitions of CO were observed in emission and absorption by Liszt & Lucas (1998), and was seen to apply even when the CO optical depths were substantial. It can be understood as the result of weak (strongly sub-thermal) rotational excitation at the

kinetic temperatures typical of diffuse molecular gas (Goldreich & Kwan 1974; Liszt 2007a).

In both panels of Figure 5, 113 UV absorption measurements of  $N(\text{CO})$  and  $N(\text{H}_2)$  are shown as a greyed background. The mm-wave measurements take several forms as noted in Section 2.2. Results based solely on  $J=1-0$  emission measurements ( $W_{\text{CO}}$ ) are plotted as pink filled rectangles with smaller symbols representing  $3\sigma$  upper limits. Six measurements of  $N(\text{CO})$  toward mm-wave background sources in Chamaeleon based on  $J=1-0$  absorption are shown as filled green rectangles, and green asterisks denote eight stellar lines of sight where  $N(\text{CO})$  and  $N(\text{H}_2)$  were measured in UV absorption toward stars in Chamaeleon (Liszt et al. 2018b). The  $N(\text{CO})$  values of Liszt & Lucas (1998) based on  $J=1-0$  and  $J=2-1$  absorption and emission measurements are shown as brown filled diamonds.

At left in Figure 5 the vertical scale is  $N(\text{CO})$  and shaded dashed lines represent the fractional abundance  $N(\text{CO})/N(\text{H}_2)$ . The vertical scale at right is in units of integrated brightness,  $\text{K-km s}^{-1}$ , and the shaded dashed lines in the right panel represent  $N(\text{H}_2)/W_{\text{CO}}$ , the  $\text{CO-H}_2$  conversion factor. Shown in both panels for reference as a shaded dash-dotted line is the power-law regression line fit to the UV absorption data at  $N(\text{H}_2) \geq 7 \times 10^{19} \text{ cm}^{-2}$  that has  $N(\text{CO}) \propto N(\text{H}_2)^{2.12}$ .

The radio data inhabit those portions of the plane above the regression line for the UV data and are much more tightly correlated with  $N(\text{H}_2)$  than are the UV data. The slope of a power-law regression line through the radio data,  $W_{\text{CO}} = 0.0030 \text{ K-km s}^{-1} (N(\text{H}_2)/10^{19} \text{ cm}^{-2})^{1.556}$ , is less steep. Unlike in the UV, there are no sightlines observed in the radio with  $N(\text{H}_2) \gtrsim 2 \times 10^{20} \text{ cm}^{-2}$  and  $N(\text{CO})/N(\text{H}_2) < 10^{-6}$ . This difference is common to all the radio datasets, representing not only the scaled  $W_{\text{CO}}$  measurements in pink but the CO column densities directly determined at radio wavelengths using CO absorption (Liszt & Lucas 1998; Liszt et al. 2018b).

Moving the radio values of  $N(\text{CO})$  to the right in Figure 5 to align them with the regression line of the UV absorption measurements would require an increase in  $N(\text{H}_2)$  by a factor  $\approx 1.6 = 0.2$  dex, ie a decrease in the  $N(\text{HCO}^+)/N(\text{H}_2)$  relative abundance of the same size. This is at the edge of the range believed to apply to empirical determination of  $N(\text{HCO}^+)/N(\text{H}_2)$  as estimated by Gerin et al. (2019). It would introduce a noticeable displacement between the UV and radio values for  $N(\text{H}_2)/E(\text{B-V})$  whose good agreement was discussed in Section 4.1.

Moving the radio datapoints vertically downward would require a factor three smaller  $N(\text{CO})/W_{\text{CO}}$  ratio that can be excluded on physical grounds if the CO emission originates in diffuse molecular gas. As discussed by Liszt (2017) the conversion  $N(\text{CO})/W_{\text{CO}} = 10^{15} \text{ cm}^{-2}/\text{K-km s}^{-1}$  is a broad local minimum with respect to the number density in calculations of the rotational excitation.  $N(\text{CO})/W_{\text{CO}}$  will increase for  $n(\text{H}) \lesssim 50 \text{ cm}^{-3}$  to compensate for the small amounts of energy being deposited in CO by collisions. At very high  $n(\text{H}) \gtrsim 1000 \text{ cm}^{-3}$  collisions will increasingly populate rotational energy levels above  $J=1$ , also increasing  $N(\text{CO})/W_{\text{CO}}$ .

The difference in behaviour between the UV and radio data in Figure 5 stands in contrast to the similar behaviour of  $N(\text{H}_2)$  vs  $E(\text{B-V})$  in Figure 4 where both the UV and radio datasets contain sightlines with small  $N(\text{H}_2)/E(\text{B-V})$ , even with appreciable reddening. But CO observed at radio wavelengths also differs from that observed in UV absorption in having more fractionation from  $\text{C}^+$  isotope exchange (Liszt 2017). The differences in the behaviour of the radio and UV datasets in Figure 5 are real, not artifacts of the scalings and proxy relationships.

As discussed by Sheffer et al. (2008), the CO column density for given  $N(\text{H})$  and  $N(\text{H}_2)$  strongly depends on the local UV radiation field, with larger CO columns for a lower radiation field. As CO is shielded by dust, by  $\text{H}_2$  and by itself for larger

N(CO) (Visser et al. 2009), the somewhat larger N(CO) and N(<sup>13</sup>CO)/N(CO) of the radio samples may be due to small variations in the sampled environments due to differences in the selection criteria of the background sources and the intrinsic variability of conditions in the diffuse interstellar gas (Hu et al. 2021).

#### 4.3. The CO-H<sub>2</sub> conversion factor

As indicated in Figure 5, equivalence of  $W_{\text{CO}}$  and N(CO) in diffuse molecular gas creates an equivalence between the CO relative abundance N(CO)/N(H<sub>2</sub>) and the CO-H<sub>2</sub> conversion factor  $\alpha = \text{N(H}_2\text{)}/W_{\text{CO}}$ . There is a wide variation in  $\alpha$  observed at radio wavelengths and an even larger implied variation in the UV absorption data. Nevertheless, the ensemble mean  $\langle \text{N(H}_2\text{)}/\langle W_{\text{CO}} \rangle \rangle = 2.4 \times 10^{20} \text{H}_2 \text{ (K-km s}^{-1}\text{)}^{-1}$  or  $= 2.1 \times 10^{20} \text{H}_2 \text{ (K-km s}^{-1}\text{)}^{-1}$  when only the data with  $W_{\text{CO}} \geq 1 \text{ K-km s}^{-1}$  is considered. This is the same result reached on other grounds without relying on the relative abundance of HCO<sup>+</sup> by Liszt et al. (2010): the mean CO-H<sub>2</sub> conversion factor in the diffuse molecular gas is just the usual standard value<sup>1</sup>. A physical explanation offered by Liszt et al. (2010) for this coincidence noted that the small relative abundance of CO, here  $\langle \text{N(CO)}/\text{N(H}_2\text{)} \rangle = 4 \times 10^{-6}$ , is compensated by a very high brightness per CO molecule  $W_{\text{CO}}/\text{N(CO)} = 1 \text{ K-km s}^{-1} \times \text{N(CO)}/10^{15} \text{ cm}^{-2}$  in the J=1-0 line, resulting from the strongly sub-thermal excitation.

#### 4.4. The molecular fraction of gas observed in CO emission

Mean molecular fractions  $\langle f_{\text{H}_2} \rangle = 0.2 - 0.24$  were derived in Section 3.3 for the lines of sight sampled in H<sub>2</sub> in UV absorption, as shown in Table 3. This is the same value suggested by the

original *Copernicus* sample after correction for a bias toward low mean line of sight density and low molecular fraction (Bohlin et al. 1978). The molecular fraction of the gas observed in HCO<sup>+</sup> absorption is higher, 0.25-0.35 for N(H)/E(B-V) =  $6-8.3 \times 10^{21} \text{ cm}^{-2} \text{ mag}^{-1}$ , as also shown in Table 3.

The CO-H<sub>2</sub> conversion factor can be used to constrain the mean molecular fraction in the diffuse molecular gas where CO emission was observed. Expressing  $\text{N(H)} = \beta \text{E(B-V)}$  and  $\text{N(H}_2\text{)} = f_{\text{H}_2} \text{N(H)}/2$ , we have  $\text{N(H}_2\text{)}/W_{\text{CO}} = (\beta f_{\text{H}_2}/2) \text{E(B-V)}/W_{\text{CO}}$ . The variation of  $W_{\text{CO}}$  with E(B-V) is shown in Figure 6: For the 58 sightlines observed in CO emission at  $\text{E(B-V)} \geq 0.07 \text{ mag}$ , taking upper limits on  $W_{\text{CO}}$  at their  $3\sigma$  values, one has  $\langle W_{\text{CO}} \rangle = 2.492 \text{ K-km s}^{-1}$  and  $\langle \text{E(B-V)} \rangle = 0.529 \text{ mag}$ . With  $\beta = 6.2 \times 10^{21} \text{ H-nuclei cm}^{-2} \text{ (mag)}^{-1}$  the implied mean molecular fraction in the CO-detected gas is 0.34, near the upper end of the range in Table 4 based on E(B-V) and N(H<sub>2</sub>) alone. This higher mean molecular fraction in gas observed away from bright stars could account for the occurrence of the radio CO data in Figure 5 above the regression line for the CO observed in UV absorption.

## 5. SUMMARY

We began by noting the complementary nature of UV/optical and radio observations of diffuse, partially molecular interstellar gas. The rich polyatomic chemistry of diffuse molecular gas is only apparent in absorption at radio wavelengths but the column densities of atomic and molecular hydrogen determined in UV absorption provide a characterization of the host gas that is not matched in the radio domain. Observations in common of CH, CO and OH provide the rudiments of a bridge between the radio and UV/optical domains and determinations of reddening E(B-V) are available through different means, which we use throughout this work.

Prior observations indicated that the relative abundance of the widely observable polyatomic

<sup>1</sup> Lada & Dame (2020) recently revised the local value of the CO-H<sub>2</sub> conversion factor upward by a factor 1.8 to  $\text{N(H}_2\text{)}/W_{\text{CO}} = 3.6 \times 10^{20} \text{H}_2 \text{ cm}^{-2} \text{ (K-km s}^{-1}\text{)}^{-1}$ . This is close to the originally-suggested but subsequently-eclipsed value  $\text{N(H}_2\text{)}/W_{\text{CO}} = 5 \times 10^{20} \text{H}_2 \text{ cm}^{-2} \text{ (K-km s}^{-1}\text{)}^{-1}$  of Liszt (1982).

**Table 1.** Line of sight properties and new results for HCO<sup>+</sup> and CO

Source	RA(J2000) hh.mmss	Dec(J2000) dd.mmss	$l$ degrees	$b$ degrees	E(B-V) mag	flux Jy	$\Upsilon_{\text{HCO}^+}^2$ km s <sup>-1</sup>	$\sigma \Upsilon_{\text{HCO}^+}$ km s <sup>-1</sup>	$W_{\text{CO}}$ K-km s <sup>-1</sup>
J0203+1134 <sup>1</sup>	2.03464	11.34492	149.6826	-47.4992	0.144	0.126	≤0.263	0.088	
J0209+1352	2.09357	13.52045	150.1800	-44.8290	0.094	0.223	0.20	0.050	≤0.071
J0211+1051	2.11132	10.51348	152.5781	-47.3674	0.145	0.462	0.76	0.029	0.36
J0213+1820	2.13105	18.20255	148.7289	-40.4014	0.130	0.093	≤0.345	0.115	
J0231+1322	2.31459	13.22547	157.0917	-42.7380	0.121	0.430	0.14	0.025	≤0.064
J0242+1742	2.42243	17.42589	157.0180	-37.7033	0.077	0.227	≤0.151	0.050	
J0252+1718	2.52077	17.18427	159.7420	-36.7885	0.220	0.172	0.25	0.077	≤0.096
J0325+2224	3.25368	22.24004	163.6700	-28.0213	0.213	1.162	1.01	0.017	0.94
J0329+3510	3.29154	35.10060	155.9152	-17.4042	0.267	0.570	0.51	0.032	≤0.143
J0329+2756	3.29577	27.56155	160.7030	-23.0743	0.198	0.158	≤0.193	0.064	
J0334+0800	3.34533	8.00144	177.2396	-37.0871	0.391	0.150	0.44	0.088	≤0.162
J0336+3218	3.36301	32.18293	158.9998	-18.7650	0.733	1.689	0.16	0.009	≤0.219
J0356+2903	3.56085	29.03423	164.6120	-18.4927	0.212	0.139	1.50	0.090	1.62
J0357+2319	3.57216	23.19538	169.0302	-22.4661	0.185	0.224	0.28	0.027	≤0.192
J0400+0550	4.00117	5.50431	184.2710	-33.7266	0.266	0.159	0.25	0.063	≤0.172
J0401+0413	4.01199	4.13344	186.0261	-34.4947	0.341	0.405	0.49	0.021	0.19
J0403+2600	4.03056	26.00015	168.0260	-19.6483	0.201	0.331	0.60	0.029	0.62
J0406+0637	4.06343	6.37150	184.7075	-32.0009	0.283	0.264	0.54	0.051	0.63
J0407+0742	4.07291	7.42075	183.8723	-31.1558	0.265	0.387	0.53	0.031	0.19
J0426+0518	4.26366	5.18199	189.3631	-28.7705	0.291	0.516	0.12	0.020	≤0.170
J0426+2327	4.26557	23.27396	173.8881	-17.4457	0.539	0.304	2.57	0.057	4.84
J0427+0457	4.27476	4.57083	189.8857	-28.7306	0.335	0.414	0.62	0.024	0.39
J0437+2037	4.31038	20.37343	176.8096	-18.5565	0.532	0.217	1.54	0.073	0.67
J0431+1731	4.31574	17.31358	179.4942	-20.3579	0.464	0.104	1.01	0.110	0.70
J0433+0521	4.33111	5.21156	190.3730	-27.3967	0.298	4.911	0.35	0.003	≤0.109
J0437+2940	4.37044	29.40138	170.5818	-11.6609	0.979	0.059	5.92	1.138	10.42
J0438+3004	4.38049	30.04455	170.4116	-11.2283	0.952	0.689	6.25	0.038	7.11
J0439+3045	4.39178	30.45076	170.0655	-10.5913	0.867	0.195	5.05	0.082	6.69
J0440+1437	4.40211	14.37570	183.2538	-20.5438	0.681	0.337	1.21	0.031	0.83
J0445+0715	4.45014	7.15539	190.4535	-23.8898	0.121	0.275	≤0.083	0.028	
J0449+1121	4.49077	11.21286	187.4274	-20.7365	0.504	0.521	0.65	0.022	0.23
J0502+1338	5.02332	13.38110	187.4143	-16.7456	0.564	0.271	1.81	0.059	2.46
J0510+1800	5.10024	18.00416	184.7304	-12.7895	0.328	2.411	0.13	0.005	0.17

<sup>1</sup> The coordinates of J0203+1134 should be read as 2<sup>h</sup>03<sup>m</sup>46.4<sup>s</sup>, 11°34′49.2″<sup>2</sup>  $\Upsilon_{\text{HCO}^+}$  is the integrated optical depth of HCO<sup>+</sup> in units of km s<sup>-1</sup>

**Table 2.** E(B-V) and N(HI) at E(B-V) ≤ 0.08 mag

sample	n	<E(B-V)> mag	<N(HI)> cm <sup>-2</sup>	<N(HI)>/<E(B-V)> cm <sup>-2</sup> mag <sup>-1</sup>
<a href="#">Bohlin et al. (1978)</a> etc. <sup>1</sup>	26	0.0569	2.332×10 <sup>20</sup>	4.10×10 <sup>21</sup>
<a href="#">Diplas &amp; Savage (1994)</a>	50	0.0526	3.563×10 <sup>20</sup>	6.77×10 <sup>21</sup>
<a href="#">Gillmon et al. (2006)</a> <sup>2</sup>	34	0.0348	2.409×10 <sup>20</sup>	6.92×10 <sup>21</sup>
Two above	84	0.0454	3.096×10 <sup>20</sup>	6.82×10 <sup>21</sup>
All E(B-V) ≤ 0.08 mag	111	0.0477	2.949×10 <sup>20</sup>	6.18×10 <sup>21</sup>

<sup>1</sup> Results from [Bohlin et al. \(1978\)](#), [Burgh et al. \(2007\)](#) and [Shull et al. \(2021\)](#) in Figure 2 at right

<sup>2</sup> Sightlines with measured N(HI), ignoring toward NGC 1068 (see Figure 2)

**Table 3.** Survey mean and ensemble parameters

Source for N(H <sub>2</sub> )	n <sup>1</sup>	<E(B-V)> mag	<N(H <sub>2</sub> )> log cm <sup>-2</sup>	<N(H <sub>2</sub> )>/<E(B-V)> log cm <sup>-2</sup> mag <sup>-1</sup>	<f <sub>H<sub>2</sub></sub> >	<N(H)>/<E(B-V)> 10 <sup>21</sup> cm <sup>-2</sup> mag <sup>-1</sup>
<a href="#">Bohlin et al. (1978)</a>	76	0.212	20.040	20.710	0.177	5.41
<a href="#">Gillmon et al. (2006)</a>	38	0.041	18.753	20.141	0.040	6.88
<a href="#">Burgh et al. (2007)</a>	24	0.349	20.458	20.915	0.225	7.30
<a href="#">Sheffer et al. (2008)</a>	64	0.339	20.497	20.967	0.267	6.66
<a href="#">Rachford et al. (2009)</a>	38	0.519	20.791	21.075	0.370	6.43
<a href="#">Shull et al. (2021)</a>	112 <sup>2</sup>	0.396	20.412	20.814	0.215	5.95
All UV	378	0.323	20.40	20.89	0.213	6.13
Radio unflagged <sup>3</sup>	88	0.563	20.772	21.02	0.253-0.350 <sup>4</sup>	
Radio flagged <sup>4</sup>	71	0.674	20.862	21.03	0.260-0.359 <sup>5</sup>	

<sup>1</sup> Numbers of targets with measured N(H<sub>2</sub>)

<sup>2</sup> 112 targets had measured N(HI) and N(H<sub>2</sub>)

<sup>3</sup> Upper limits are taken at the 3σ value

<sup>4</sup> Sightlines with upper limits are ignored

<sup>5</sup> For N(H)/<E(B-V)> = 6 – 8.3 × 10<sup>21</sup> cm<sup>-2</sup> mag<sup>-1</sup>



ion  $\text{HCO}^+$  is constant in diffuse molecular gas, with  $N(\text{HCO}^+)/N(\text{H}_2) = 3 \times 10^{-9}$ . In that case,  $E(\text{B-V})$  and  $N(\text{HCO}^+)$ , together with the usual assumed total hydrogen/reddening ratio  $N(\text{H})/E(\text{B-V})$ , give the relative abundances of molecules with respect to  $\text{H}_2$  and the fraction of H-nuclei in  $\text{H}_2$ ,  $f_{\text{H}_2} = 2N(\text{H}_2)/N(\text{H})$ . In turn, mm-wave observations of CO in emission determine the CO- $\text{H}_2$  conversion factor in the diffuse molecular gas.

Our focus, then, was on three aspects of the observations: determining  $N(\text{HI})/E(\text{B-V})$  and  $N(\text{H}) = N(\text{HI}) + 2N(\text{H}_2)/E(\text{B-V})$  (Figures 1-3 and Tables 2-3 and 5); comparing  $N(\text{H}_2)$  and  $E(\text{B-V})$  measured at UV and radio wavelengths; and comparing observed and implied column densities  $N(\text{CO})$  and integrated  $J=1-0$  brightnesses  $W_{\text{CO}}$  of carbon monoxide.

We first discussed the  $N(\text{H})/E(\text{B-V})$  ratio that was originally determined in optical UV/absorption by *Copernicus* to be  $N(\text{H}) = 5.8 \times 10^{21} \text{ H-nuclei cm}^{-2} (\text{mag})^{-1}$  but subsequently was found to be globally larger,  $8.3 \times 10^{21} \text{ H-nuclei cm}^{-2} (\text{mag})^{-1}$ , at high galactic latitude when deriving  $N(\text{HI})$  from  $\lambda 21\text{cm}$  emission and  $E(\text{B-V})$  from scaled far-IR emission. The tension between these values is not resolved by the vastly increased number of UV-absorption measurements undertaken subsequent to *Copernicus*. Overall and especially at  $E(\text{B-V}) \gtrsim 0.1 \text{ mag}$  where the molecular fraction is appreciable and the plot of  $N(\text{H})$  vs  $E(\text{B-V})$  wraps itself tightly about the regression line in Figure 1, we find that  $N(\text{H}) = 6.2 \times 10^{21} \text{ H-nuclei cm}^{-2} (\text{mag})^{-1}$  is a good average for sightlines with  $N(\text{H}_2)$  measured in UV absorption.

That said,  $\langle N(\text{HI}) \rangle / \langle E(\text{B-V}) \rangle$  and the scatter in  $N(\text{HI})$  vs  $E(\text{B-V})$  are larger at  $E(\text{B-V}) < 0.08 \text{ mag}$  (Figure 1) where there is no competition for H-nuclei between atomic and molecular hydrogen. In Figure 2 and Tables 2 and 5 we remarked several properties of the UV absorption measurements at  $E(\text{B-V}) \leq 0.08 \text{ mag}$  of  $N(\text{HI})$  subsequent to *Copernicus*: they have an HI/reddening ratio

$\langle N(\text{HI}) \rangle / \langle E(\text{B-V}) \rangle = 6.8 \times 10^{21} \text{ H-nuclei cm}^{-2} (\text{mag})^{-1}$  that is much larger than in the *Copernicus* sample ( $4.1 \times 10^{21} \text{ H-nuclei cm}^{-2} (\text{mag})^{-1}$  in Table 2) but is equal to the ratio seen toward optically bright AGN when  $N(\text{HI})$  is measured in  $\lambda 21\text{cm}$  emission and  $E(\text{B-V})$  is inferred from far-IR emission ( $6.9 \times 10^{21} \text{ H-nuclei cm}^{-2} (\text{mag})^{-1}$ ). Similarity of the mean values of  $\langle N(\text{HI}) \rangle / \langle E(\text{B-V}) \rangle$  in these post-*Copernicus* samples suggests that scatter in the plot of stellar measurements of  $N(\text{HI})$  vs  $E(\text{B-V})$  is due to errors in the stellar photometry that is demonstrated in Appendix C and Figure 8. Subdividing the stellar absorption data into subsamples of common and unshared sightlines at small and large reddening in Appendix C showed no calibration differences in measured  $N(\text{HI})$  but notable differences in  $E(\text{B-V})$  for shared sightlines at low  $E(\text{B-V})$ , and very different explanations for disparities in  $N(\text{HI})/E(\text{B-V})$  in the same sense.

In Figure 4 we merged the radio and UV determinations of  $N(\text{H}_2)$  and jointly plotted them against  $E(\text{B-V})$ . They coincide and have comparable scatter when  $\text{H}_2$  is detected. They also do not contradict each other at low reddening where  $N(\text{H}_2)$  is small and  $\text{HCO}^+$  is not detected (Table 3). Thus, radio and optical data provide the same view of the  $\text{HI} \rightarrow \text{H}_2$  transition in diffuse gas and a numerical comparison is given in Table 3. This commensurability is gratifying and lends confidence to the use of  $N(\text{HCO}^+)/N(\text{H}_2) = 3 \times 10^{-9}$  along sightlines observed at radio wavelengths. It has the consequence that if  $N(\text{HCO}^+)$  is measured and  $N(\text{H}_2)$  is derived indirectly by some other means, the implied relative abundance  $N(\text{HCO}^+)/N(\text{H}_2)$  should be consistent with  $3 \times 10^{-9}$ . Possible use cases are when  $E(\text{B-V})$  is scaled to  $N(\text{H})$  and a value of  $N(\text{HI})$  is subtracted to determine  $N(\text{H}_2)$  or when  $W_{\text{CO}}$  is scaled to  $N(\text{H}_2)$  and subtracted from  $N(\text{H})$  to find  $N(\text{HI})$  and  $f_{\text{H}_2}$ .

We merged the UV and radio determinations of  $N(\text{CO})$  and plotted them against  $N(\text{H}_2)$  in Figure 5, testing the equivalence of  $W_{\text{CO}}$  and  $N(\text{CO})$ ,  $W_{\text{CO}} = N(\text{CO})/10^{15} \text{ cm}^{-2} \text{ K-km s}^{-1}$ . This was first ob-

served when  $N(\text{CO})$  was derived by observing CO emission and absorption in the lower rotation levels, and it applies even to optically thick CO lines over the observed range of  $N(\text{CO}) \lesssim 10^{16} \text{ cm}^{-2}$ . It can be understood by realizing that photons eventually escape after scattering in a medium where the excitation of CO is weak (significantly sub-thermal), even when the  $J=1-0$  line is optically thick.

Here a difference was found: The radio and UV data overlap but the radio data inhabit only the upper portions of the region in the  $N(\text{CO})$ - $N(\text{H}_2)$  plane that are occupied by the UV data. Unlike in the UV, sightlines are not present in the radio dataset with  $N(\text{H}_2) \gtrsim 2 \times 10^{20} \text{ cm}^{-2}$  and  $N(\text{CO}) < 10^{14} \text{ cm}^{-2}$  or  $N(\text{CO})/N(\text{H}_2) < 10^{-6}$ . In Section 4.4 we noted that the molecular fraction appears to be higher in the gas observed in CO emission and  $\text{HCO}^+$  absorption, 0.34 vs 0.22.

Radio measurements of  $W_{\text{CO}}$  are much more tightly correlated with  $N(\text{HCO}^+)$  than are  $N(\text{CO})$  and  $N(\text{H}_2)$  measured in UV absorption. Overall, there is a power-law relation between  $W_{\text{CO}}$  and  $N(\text{H}_2)$  measured in the radio domain  $W_{\text{CO}} = 0.0030 \text{ K-km s}^{-1} (N(\text{H}_2)/10^{19} \text{ cm}^{-2})^{1.556}$ .

Variations in  $N(\text{CO})/N(\text{H}_2)$  (Figure 5) and  $N(\text{H}_2)/E(\text{B-V})$  (Figure 1) drive variations in  $N(\text{H}_2)/W_{\text{CO}}$  (aka the CO-H<sub>2</sub> conversion factor) and  $W_{\text{CO}}/E(\text{B-V})$  (Figure 6). Nonetheless, the overall ensemble mean for the radio data discussed in Section 4.3,  $\langle N(\text{H}_2) \rangle / \langle W_{\text{CO}} \rangle = 2.1 - 2.4 \times 10^{20} \text{ H}_2 \text{ cm}^{-2} (\text{K-km s}^{-1})^{-1}$ , is like those in common use in dense and dark gas,  $W_{\text{CO}}/N(\text{H}_2) = 2 - 4 \times 10^{20} \text{ H}_2 \text{ cm}^{-2} (\text{K-km s}^{-1})^{-1}$ . In statistical terms, this similarity in the ensemble mean arises because so much of the CO emission is contributed by lines of sight at higher  $E(\text{B-V})$  where the relative CO

abundance is higher. In terms of the physics, similarity of the CO-H<sub>2</sub> conversion factors in diffuse and fully molecular dense gas arises from compensating influences of the CO chemistry and excitation: The smaller relative abundance  $N(\text{CO})/N(\text{H}_2)$  in low density diffuse molecular gas is compensated by a high brightness in the  $J=1-0$  line per CO molecule ( $W_{\text{CO}}/N(\text{CO})$ ) resulting from the strongly sub-thermal excitation.

The National Radio Astronomy Observatory is a facility of the National Science Foundation operated under contract by Associated Universities, Inc. This work was supported in part by the Programme National “Physique et Chimie du Milieu Interstellaire” (PCMI) of CNRS/INSU with INC/INP co-funded by CEA and CNES.

This work is based in part on observations carried out under project number 003-19 with the IRAM 30m telescope. IRAM is supported by INSU/CNRS (France), MPG (Germany) and IGN (Spain). The assistance of the IRAM staff and, especially, help from Axel García Rodríguez, is very much appreciated.

This paper makes use of the following ALMA data: ADS/JAO.ALMA#2018.1.00115.S, ADS/JAO.ALMA#2017.1.00120.S and ADS/JAO.ALMA#2016.1.00714.S. ALMA is a partnership of ESO (representing its member states), NSF (USA) and NINS (Japan), together with NRC (Canada), NSC and ASIAA (Taiwan), and KASI (Republic of Korea), in cooperation with the Republic of Chile. The Joint ALMA Observatory is operated by ESO, AUI/NRAO and NAOJ.

We thank Isabelle Grenier for comments on earlier versions of this work and we thank the referee, Michael Shull, for many helpful remarks.

## APPENDIX

**Table 4.** Sources for Column Densities and Reddening

Reference	E(B-V)	N(HI)	N(H <sub>2</sub> )	N(CO)
Burgh et al. (2007)	Stellar Photometry	UV Absorption	UV Absorption	UV Absorption
Sheffer et al. (2008)	''	''	''	''
Rachford et al. (2009)	''	''	''	''
Shull et al. (2021)	''	''	''	''
Bohlin et al. (1978)	''	''	''	NA
Diplas & Savage (1994)	''	''	NA	NA
Gillmon et al. (2006)	Schlegel et al. (1998)	$\lambda$ 21cm emission	UV Absorption	NA
Liszt & Lucas (1998)	''	NA	Scaled HCO <sup>+</sup>	mm-wave emission & absorption
Liszt et al. (2019)	''	NA	''	mm-wave absorption

### A. SOURCES FOR COLUMN DENSITIES AND REDDENING

Shown in Table 4 are the sources and methods by which reddenings and column densities were derived for references cited here for their measurement of N(HI), N(H<sub>2</sub>) and N(CO).

### B. SPECTRA OF HCO<sup>+</sup> AND CO

Spectra of HCO<sup>+</sup> and CO in the 28 directions with detected HCO<sup>+</sup> absorption are shown in Figure 7. The HCO<sup>+</sup> absorption is the negative-going signal shown in red. The black histogram shows the CO emission. The as-delivered frequency-switched IRAM 30m CO spectra were, unfortunately, already folded in frequency, preventing a separation of the phases of the frequency switching cycle using the methods of Liszt (1997). Only the positive-going signal coincident with HCO<sup>+</sup> absorption is interstellar, signals at the 0.5 - 1 K level not coincident with HCO<sup>+</sup> is telluric.

### C. STELLAR DETERMINATIONS OF N(HI) AND E(B-V) AT LOW E(B-V)

The discussion in Section 3, along with Figure 2 and the numerical results in Table 2, showed a significant disparity between the N(HI)/E(B-V) ratios measured toward stars by Diplas & Savage (1994) and Bohlin et al. (1978) at  $E(B-V) \leq 0.08$  mag where  $f_{H_2}$  is negligible. Meanwhile, Gillmon et al. (2006) arrived at the same N(HI)/E(B-V) as Diplas & Savage (1994) while deriving E(B-V) from Schlegel et al. (1998) and N(HI) from  $\lambda$ 21cm emission, with much smaller scatter in the plot of N(HI) vs E(B-V) (Figure 2). In Section 3.1 we ascribed the larger scatter in the stellar measurements of N(HI)/E(B-V) to error in the photometric determination of E(B-V) that is consistent with having the same mean.

Shown in Figure 8 are the measurements of N(HI) and N(HI)/E(B-V) for sightlines in common between Bohlin et al. (1978) and Diplas & Savage (1994): 15 and 13 stars respectively for which  $E(B-V) \leq 0.08$  mag in either dataset and 63 stars in common overall. Comparison of the tightly correlated plots of column density at left with the plots of column density/reddening ratio at right clearly show the scatter introduced by differences in the stellar reddening.

Numerical results are abstracted in Table 5 for increasingly larger samples from both datasets. Results for the 63 common sightlines should serve as a fiducial and they show agreement in the mean E(B-V) and N(HI) at the 1% level. This overall agreement renders the results at low E(B-V) somewhat confounding. *Considering only the data at  $E(B-V) \leq 0.08$  mag*, the much larger N(HI)/E(B-V) in Diplas & Savage (1994) along common sightlines arises from a difference in E(B-V) with nearly equal N(HI), while for the whole

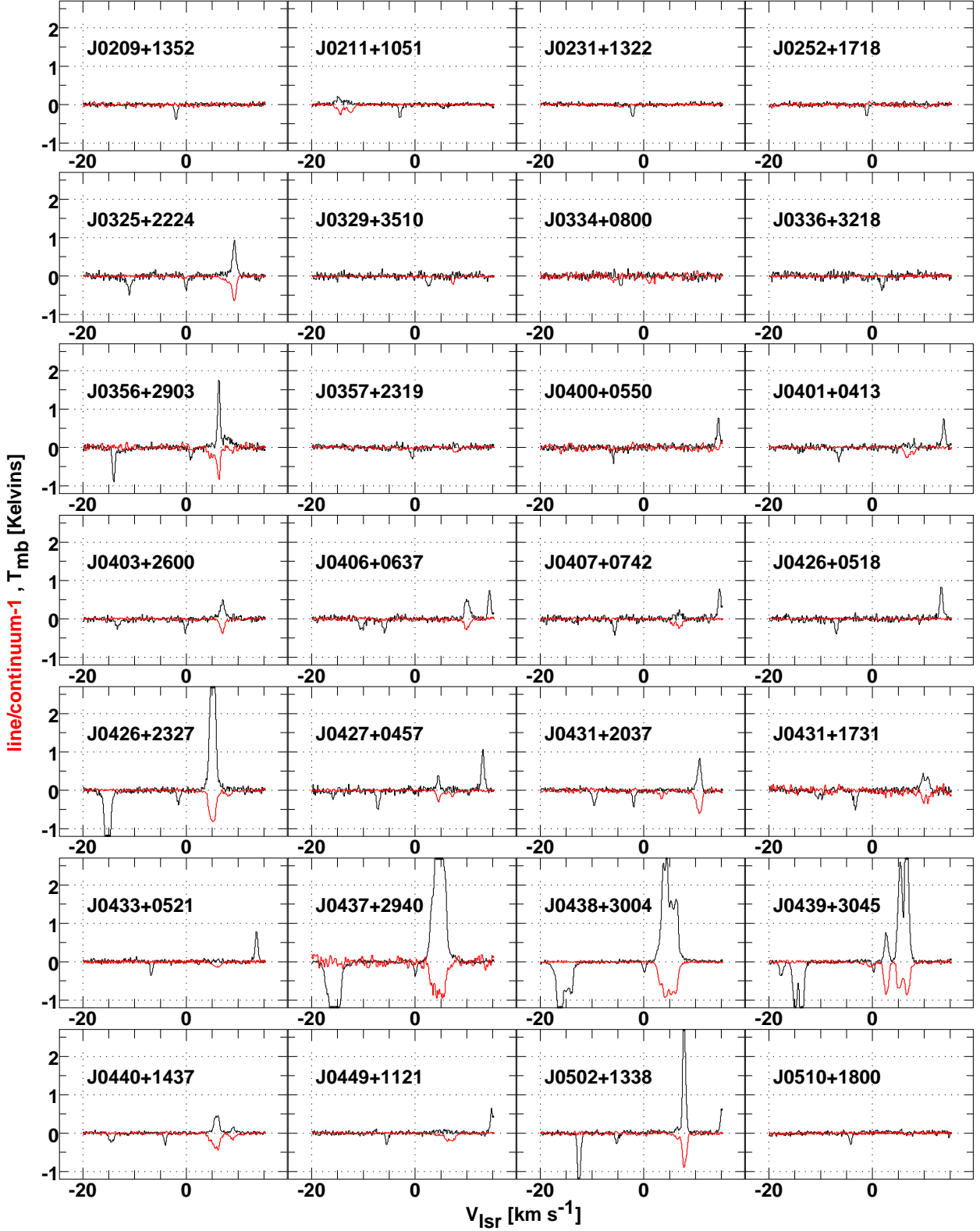


**Figure 7.** Spectra of HCO<sup>+</sup> absorption (red) and CO emission (black) from the Galactic anticenter sample. See Appendix B for an explanation of the appearance of the frequency-switched IRAM 30m emission spectra.

**Table 5.** E(B-V) and N(HI) at E(B-V)  $\leq$  0.08 mag and in general

Authors	sub-sample	n	$\langle E(B-V) \rangle$ mag	$\langle N(HI) \rangle$ $10^{20} \text{ cm}^{-2}$	$\langle N(HI) \rangle / \langle E(B-V) \rangle$ $10^{21} \text{ cm}^{-2} \text{ mag}^{-1}$
Bohlin et al. (1978)	Common E(B-V) $\leq$ 0.08 mag	15	0.069(0.015)	2.69(1.25)	3.90
Diplas & Savage (1994)	”	13	0.054(0.015)	2.80(1.28)	5.20
Bohlin et al. (1978)	Unique E(B-V) $\leq$ 0.08 mag	11	0.041(0.025)	1.85(1.96)	3.83
Diplas & Savage (1994)	”	37	0.052(0.020)	3.83(1.75)	7.34
Bohlin et al. (1978) etc	All E(B-V) $\leq$ 0.08 mag <sup>1</sup>	26	0.057(0.024)	2.33(1.64)	4.10
Diplas & Savage (1994)	”	50	0.053(0.019)	3.56(1.70)	6.77
Bohlin et al. (1978)	All common, any E(B-V)	63	0.212(0.130)	9.55(8.73)	4.50
Diplas & Savage (1994)	”	63	0.210(0.130)	9.55(7.01)	4.55
Bohlin et al. (1978)	All in dataset	90	0.198(0.131)	8.56(7.92)	4.32
Diplas & Savage (1994)	”	388	0.312(0.180)	15.33(7.80)	4.91

<sup>1</sup> From Table 2

low reddening sample the difference arises from much larger N(HI) in [Diplas & Savage \(1994\)](#) with nearly equal E(B-V). The common sightlines have small N(HI)/E(B-V) even in [Diplas & Savage \(1994\)](#).

## REFERENCES

- Bellomi, E., Godard, B., Hennebelle, P., et al. 2020, A&A, 643, A36
- Bohlin, R. C., Savage, B. D., & Drake, J. F. 1978, ApJ, 224, 132
- Burgh, E. B., France, K., & McCandliss, S. R. 2007, ApJ, 658, 446
- Cox, P., Güsten, R., & Henkel, C. 1988, A&A, 206, 108
- Diplas, A. & Savage, B. D. 1994, ApJ, 427, 274
- Geballe, T. R. & Oka, T. 1996, Natur, 384, 334
- Gerin, M. & Liszt, H. 2021, A&A, 648, A38
- Gerin, M., Liszt, H., Neufeld, D., et al. 2019, A&A, 622, A26
- Gerin, M., Neufeld, D. A., & Goicoechea, J. R. 2016, ARA&A, 54, 181
- Gillmon, K., Shull, J. M., Tumlinson, J., & Danforth, C. 2006, ApJ, 636, 891
- Goldreich, P. & Kwan, J. 1974, ApJ, 189, 441
- Gudennavar, S. B., Bubbly, S. G., Preethi, K., & Murthy, J. 2012, ApJS, 199, 8
- Hensley, B. S. & Draine, B. T. 2017, ApJ, 836, 179
- . 2021, ApJ, 906, 73
- Hu, C.-Y., Sternberg, A., & van Dishoeck, E. F. 2021, ApJ, 920, 44
- Lada, C. J. & Dame, T. M. 2020, ApJ, 898, 3
- Lenz, D., Hensley, B. S., & Doré, O. 2017, ApJ, 846, 38
- Li, D., Tang, N., & Nguyen, H. 2018, ApJS, 235, 1
- Liszt, H. 1997, A&A. Supp., 124, 183
- . 2014a, ApJ, 783, 17
- . 2014b, ApJ, 780, 10
- . 2021, arXiv e-prints, arXiv:2104.15013
- Liszt, H. & Gerin, M. 2018, A&A, 610, A49
- Liszt, H., Gerin, M., Beasley, A., & Pety, J. 2018a, ApJ, 856, 151
- Liszt, H., Gerin, M., & Grenier, I. 2018b, A&A, 617, A54
- . 2019, A&A, 627, A95
- Liszt, H., Lucas, R., & Pety, J. 2006, A&A, 448, 253
- Liszt, H., Sonnentrucker, P., Cordiner, M., & Gerin, M. 2012, ApJ, 753, L28
- Liszt, H. S. 1982, ApJ, 262, 198
- . 2007a, A&A, 476, 291
- . 2007b, A&A, 461, 205
- . 2017, ApJ, 835, 138
- . 2020, ApJ, 897, 104
- Liszt, H. S. & Lucas, R. 1998, A&A, 339, 561
- . 2000, A&A, 355, 333
- Liszt, H. S. & Pety, J. 2012, A&A, 541, A58



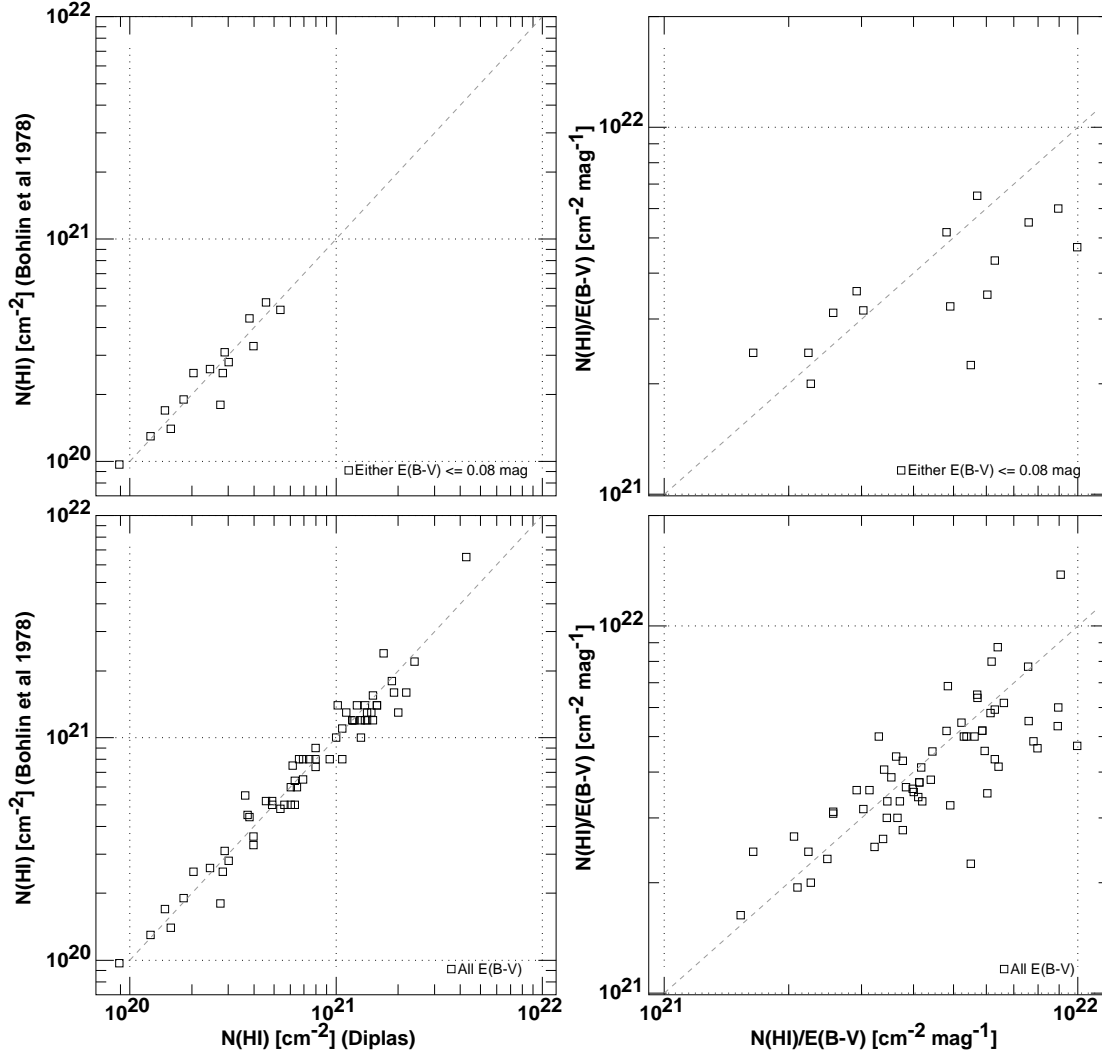


**Figure 8.** Comparison of  $N(\text{HI})$  and  $N(\text{HI})/E(B-V)$  from [Diplas & Savage \(1994\)](#) plotted horizontally and [Bohlin et al. \(1978\)](#) plotted vertically in all panels. Top: 15 common sightlines for which  $E(B-V) \leq 0.08$  in either or both datasets. Bottom: all (63) common sightlines. The gray dashed line in each panel is the locus of equal values, not a regression line.

Liszt, H. S., Pety, J., & Lucas, R. 2010, *A&A*, 518, A45+  
 Lucas, R. & Liszt, H. S. 1993, *A&A*, 276, L33  
 —. 1996, *A&A*, 307, 237  
 —. 2000, *A&A*, 358, 1069  
 —. 2002, *A&A*, 384, 1054  
 Maier, J. P., Lakin, N. M., Walker, G. A. H., & Bohlender, D. A. 2001, *ApJ*, 553, 267  
 Nash, A. G. 1990, *ApJS*, 72, 303  
 Neufeld, D. A., Godard, B., Gerin, M., et al. 2015, *A&A*, 577, A49  
 Planck Collaboration, Fermi Collaboration, Ade, P. A. R., Aghanim, N., Aniano, G., Arnaud, M., & Ashdown, M. 2015, *A&A*, 582, A31

Rachford, B. L., Snow, T. P., Destree, J. D., et al. 2009, *ApJS*, 180, 125  
 Remy, Q., Grenier, I. A., Marshall, D. J., & Casandjian, J. M. 2018, *A&A*, 611, A51  
 Savage, B. D., Drake, J. F., Budich, W., & Bohlin, R. C. 1977, *ApJ*, 216, 291  
 Schlegel, D. J., Finkbeiner, D. P., & Davis, M. 1998, *ApJ*, 500, 525  
 Sheffer, Y., Rogers, M., Federman, S. R., et al. 2007, *ApJ*, 667, 1002  
 Sheffer, Y., Rogers, M., Federman, S. R., et al. 2008, *ApJ*, 687, 1075  
 Shull, J. M., Danforth, C. W., & Anderson, K. L. 2021, *ApJ*, 911, 55

- Sonnentrucker, P., Welty, D. E., Thorburn, J. A., & York, D. G. 2007, ApJS, 168, 58
- Spitzer, L. 1978, Physical processes in the interstellar medium (New York Wiley-Interscience, 1978. 333 p.)
- Visser, R., van Dishoeck, E. F., & Black, J. H. 2009, A&A, 503, 323
- Wakker, B. P., Kalberla, P. M. W., van Woerden, H., et al. 2001, ApJS, 136, 537
- Weselak, T., Galazutdinov, G. A., Beletsky, Y., & Kr  owski, J. 2010, MNRAS, 402, 1991